Nucleation of helium in liquid lithium at 843 K and high pressures

Jordi Martí [1]*, Ferran Mazzanti[1], Grigori E.Astrakharchik[1], Lluís Batet[1], Laura Portos-Amill,[2] Borja Pedreño[2]

1   Affiliation: Department of Physics, Polytechnic University of Catalonia-Barcelona Tech, Barcelona, Catalonia,Spain.

2   Affiliation: Barcelona School of Telecommunications Engineering, Polytechnic University of Catalonia-Barcelona Tech,Barcelona, Catalonia,Spain.

*   Correspondence: jordi.marti@upc.edu

1   **Abstract:** Fusion energy stands out as a promising alternative for a future decarbonised energy
2   system. In order to be sustainable, future fusion nuclear reactors will have to produce their own
3   tritium. In the so-called breeding blanket of a reactor, the neutron bombardment of lithium will
4   produce the desired tritium, but also helium, which can trigger nucleation mechanisms owing to
5   the very low solubility of helium in liquid metals. An understanding of the underlying microscopic
6   processes is important for improving the efficiency, sustainability and reliability of the fusion energy
7   conversion process. The spontaneous creation of helium droplets or bubbles in the liquid metal used
8   as breeding material in some designs may be a serious issue for the performance of the breeding
9   blankets. This phenomenon has yet to be fully studied and understood. This work aims to provide
10 some insight on the behaviour of lithium and helium mixtures at experimentally corresponding
11 operating conditions (843 K and pressures between 10^8 and 10^{10} Pa). We report a microscopic study
12 of the thermodynamic, structural and dynamical properties of lithium-helium mixtures, as a first
13 step to the simulation of the environment in a nuclear fusion power plant. We introduce a new
14 microscopic model devised to describe the formation of helium droplets in the thermodynamic range
15 considered. Our model predicts the formation of helium droplets at pressures around 10^9 Pa, with
16 radii between 1 and 2 Å. The diffusion coefficient of lithium (2 Å^2/ps) is in excellent agreement with
17 reference experimental data, whereas the diffusion coefficient of helium is in the range of 1 Å^2/ps
18 and tends to decrease as pressure increases.

19 **Keywords:** nucleation; breeding blankets; fusion reactors; helium-lithium mixtures

1. Introduction

21 Within the framework of future energy supply, with the constraints posed by the need of
22 electrification of the final energy demand, and the quest for more sustainable power generation
23 methods in order to achieve a decarbonised electricity system, nuclear fusion energy stands out
24 as a promising alternative. The fusion reaction that results most convenient in the present state of
25 technological development is:

$$D + T \rightarrow {}^4He + n + 17.6 \text{ MeV}, \tag{1}$$

26 where 'D' stands for deuterium, 'T' for tritium and 'n' for a free neutron and where helium is a
27 by-product[1]. Deuterium is abundant in water, but tritium ($t_{1/2}$=12.3 year) must be artificially created.
28 Therefore, in order for fusion energy to be sustainable, it is necessary that tritium be produced in
29 the reactor itself. Tritium will be generated by means of the reactions of neutrons escaping from

30 the plasma with lithium in the so-called breeding blankets (see for instance[2] for an overview of
31 these relevant components in DEMO, a demonstration power plant contemplated in the European
32 Roadmap to Fusion). Breeding blankets (BB) will perform two additional functions besides producing
33 tritium: extraction of fusion heat, and shielding the magnets (superconducting coils) from the radiation
34 escaping the plasma.

35 Lithium has two natural isotopes ^{6}Li (abundance 7.5 %) and ^{7}Li (92.5 %), both producing tritium
36 when capturing a neutron[3]:

$$n + {}^6\text{Li} \rightarrow \text{T} + {}^4\text{He} + 4.78 \text{ MeV} \tag{2}$$

$$n + {}^7\text{Li} \rightarrow \text{T} + {}^4\text{He} + n - 2.47 \text{ MeV} \tag{3}$$

37 Tritium self-sufficiency will require a certain neutron multiplication in order to close the fuel cycle with
38 a net gain so that the so-called tritium breeding ratio is greater than 1. In order to fulfil their functions,
39 some BB designs feature solid (ceramic) breeders cooled by helium, while others rely on a liquid metal
40 (LM) cooled by helium or water. The LM BB designs are considering the use of lithium-lead eutectic
41 (LLE)[2,4,5]. Besides ^{7}Li, lead will provide some fast neutron multiplication (neutrons hit the walls of
42 the reaction chamber with energies bigger than 14 MeV). As shown in Eqs. (2) and (3), He is produced
43 mol-to-mol along with T. However, He is practically insoluble in the liquid metal (Henry's constant
44 for helium in Li at 843 K would be around 7×10^{-14} Pa^{-1} atomic fraction; for LLE it is estimated
45 to be lower[6]). Tritium self-sufficiency requirement is thus linked to a possible super-saturation
46 of helium in the liquid metal and, consequently, to a possible nucleation of helium in the form of
47 bubbles. This phenomenon may have a great impact in the performance of the BB: changes in the
48 magnetohydrodynamic flow, affectation of the heat transfer, and changes in the tritium migration
49 mechanisms. Other systems that could be affected by helium nucleation are, for instance, free-surface
50 Li first wall concepts[7,8] and the Li jet targets in the future International Fusion Materials Irradiation
51 Facility[9].

52 In the quest for tools to model the effect of the undesired helium bubbles being formed in
53 the blanket walls of a nuclear fusion plant, helium nucleation models must be developed. So far,
54 no experiments exist allowing to validate such models. The low solubility of He in LM makes
55 computer simulations extremely expensive when trying to capture the onset of nucleation at the design
56 operational pressures and temperatures of BB. Indeed, a rough estimation based on the Gibbs' Classical
57 Nucleation Theory[10,11] (CNT) can be done using parameters from Ref. [12]. In order to have a stable
58 bubble, a critical size must be achieved when the internal energy of the bubble is able to overcome
59 the energy needed to create the surface around it. The smaller is the critical size, the higher is the
60 supersaturation level needed to achieve it.

61 To highlight this point, we report in Fig. 1 a graphical representation of the work of formation
62 (Gibbs free energy) of a cluster of radius r_c (see [12]):

$$\Delta G_{tot} = \Delta G_{surf.} + \Delta G_{vol.} = 4\pi r_c^2 \sigma + \frac{4}{3}\pi r_c^3 \Delta g_{vol.}, \tag{4}$$

63 where σ is the surface tension and $\Delta g_{vol.}$ is the driving force for nucleation per unit volume of the new
64 phase i.e. the Gibbs free energy difference between the cluster and the dissolved states of one He atom
65 per unit volume. According to CNT it can be expressed as[13,14]:

$$\Delta g_{vol.} = \frac{-k_B T}{v_0} \ln \psi, \tag{5}$$

66 where k_B is the Boltzmann constant, T is the liquid metal bulk temperature, v_0 is the volume of one
67 He atom in the cluster and ψ is the supersaturation ratio, relating the actual He concentration to the
68 saturation concentration.

69 Given a fixed concentration of helium in the solvent, when the solubility increases (i.e. ψ decreases)
70 the critical bubble size (i.e. the radius at which the total Gibbs free energy is maximum) is larger (in

the example of Fig. 1 ψ equals 2 for a critical size of 110 atoms of helium). If the solubility is lower, the critical bubble size is smaller (in the example of Fig. 1 ψ equals 6 for a critical size of 42 atoms of helium). Thus, in order to have a stable bubble a critical size must be achieved when the internal energy in the bubble is able to overcome the energy needed to create the surface around it. The smaller the critical size (around 40 atoms in the example above), the higher the supersaturation level needed to achieve it. Consequently, a simulation involving 40 atoms of helium at 843 K and 1 bar would require almost 10^9 atoms of lithium to be in those conditions. However, at 100 GPa only around 1000 atoms of lithium would be needed.
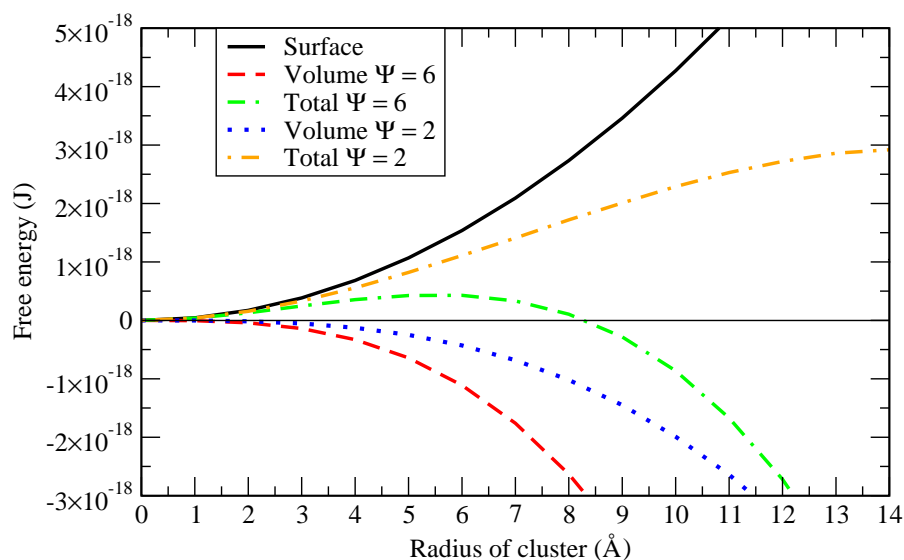
Figure 1. Free energy of a He cluster forming in lithium at 843 K assuming a surface tension of 0.34 N/m [15]. Using a volume of 17 Å^3 for helium[12] critical size is 42 atoms when supersaturation ratio $\psi = 6$ and 110 atoms when $\psi = 2$, where ψ is defined as the ratio between the actual helium concentration and the saturated concentration.

The complexity of the chemistry of the LLE system, with bred tritium and helium, including possible interactions between all types of atoms and the possibility of the formation of molecules (LiT when the eutectic composition is not well adjusted and Li_2 and T_2 in the gas phase), makes it unaffordable to try to model the interactions between all possible species at once, when the nucleation mechanism in this case has not been fully captured by models yet. For these reasons, the present work focuses on the simulation of He-Li mixtures at high pressures as a first step towards the simulation of the Li-Pb-He mixtures at low pressure. Our main goal is to capture the onset of the nucleation at a qualitative level, in order to advance towards the full modelling of the phenomenon. We describe a mixture of helium and lithium atoms in the bulk, developing a microscopic model that is able to reproduce the helium-lithium mixture instability towards nucleation of helium droplets. We thus acquire valuable structural and dynamical data from classical simulations, showing remarkable good

agreement with radial distribution functions of lithium as well as with its self-diffusion coefficient, compared to data from experimental and computational sources. Full verification of the model is limited by the current lack of available data on Li-He mixtures at high temperatures and pressures.

In particular, Li-Li, He-He and He-Li pair interactions are fed as an input to both classical Monte Carlo (MC) and molecular dynamics (MD) simulations. We find thermodynamic, structural and dynamic properties of lithium and helium mixtures at high temperatures and in a wide range of pressures between 0.1 and 10 GPa. Both MC and MD computational techniques have been previously proven to provide reliable predictions for a wide variety of classical and quantum atomic and molecular systems, ranging from pure quantum systems including hydrogen and helium[16–19] to classical molecular liquids such as water, in solution[20–22] and at interfaces[23,24] and to highly complex biosystems such as proteins or membranes[25,26]. MC and MD can be the source of mixed methods such as transition path sampling[27,28] which is able to describe the free energy hypersurface of a given statistical process without the previous knowledge of the reaction coordinates. We calculate and report thermodynamic properties such as the average internal energy as a function of pressure. To quantify the spatial and dynamical structure we calculate atomic pair distribution functions, structure factors, mean squared displacements and velocity autocorrelation functions in order to obtain atomic spectra. We also can obtain the diffusion coefficients of lithium and helium at different pressures as well as the spectral densities of He and Li, reporting information on their main translation and vibration modes.

2. Methods

Microscopic model

We base our simulations on a microscopic model Hamiltonian describing a mixture of N_{Li} lithium and N_{He} helium atoms, which are taken to be point-like particles of mass m_{Li} and m_{He}, respectively. In order to reproduce the experimental conditions, we only consider situations where $N_{\text{Li}} \gg N_{\text{He}}$. Each species is characterised by particle coordinates and velocities $\{\mathbf{r}_{\text{Li},i}, \mathbf{v}_{\text{Li},i}\}$ and $\{\mathbf{r}_{\text{He},j}, \mathbf{v}_{\text{He},j}\}$, with i and j spanning the ranges $1, \ldots, N_{\text{Li}}$ and $1, \ldots, N_{\text{He}}$, respectively. The Hamiltonian of the system is then written as

$$
\begin{aligned}
H &= \frac{1}{2}\sum_{i=1}^{N_{\text{Li}}} m_{\text{Li}} v_{\text{Li},i}^2 + \frac{1}{2}\sum_{i=1}^{N_{\text{He}}} m_{\text{He}} v_{\text{He},i}^2 \\
&+ \sum_{i<j}^{N_{\text{Li}}} V_{\text{Li}-\text{Li}}(|\mathbf{r}_{\text{Li},i}-\mathbf{r}_{\text{Li},j}|) + \sum_{i<j}^{N_{\text{He}}} V_{\text{He}-\text{He}}(|\mathbf{r}_{\text{He},i}-\mathbf{r}_{\text{He},j}|) + \sum_{i=1}^{N_{\text{Li}}}\sum_{j=1}^{N_{\text{He}}} V_{\text{Li}-\text{He}}(|\mathbf{r}_{\text{Li},i}-\mathbf{r}_{\text{He},j}|),
\end{aligned}
\tag{6}
$$

where the first two terms describe the kinetic energy, while the last three terms account for the intra- and inter-species interaction, respectively. Periodic boundary conditions are applied in order to minimise the finite-size effects and approximate better the properties of a large system. The typical simulation cage is a square box of length around 29 Å for the reference pressure of 1 GPa. At lower pressure setups, box lengths are larger than 40 Å.

A crucial point of our model is an appropriate choice of the pair interaction potentials. For lithium-lithium interactions (Eq. 7) we rely on the model proposed by Canales et al. in Ref. [29,30], whereas the remaining interactions are a novelty of the present work. The Li-Li pair potential $V(r)$ is modelled as [29,30]

$$
V_{\text{Li}-\text{Li}}(r) = Ar^{-12} + B\exp Cr \cdot \cos D(r-E),
\tag{7}
$$

where r is the distance between the two atoms in Angströms and the potential coefficients are $A = 2.22125 \times 10^7$ K Å^{12}, $B = 41828.9$ K, $C = -1.20145$ Å^{-1}, $D = 1.84959$ Å^{-1}, $E = 5.03762$ Å. This

128 potential is shown in Fig. 11, featuring strong short-distance repulsion caused by Pauli exclusion due
129 to overlapping electron orbitals, a highly non-monotonic behaviour at the distances around the van
130 der Waals radii and an attractive long-range tail. In particular, the characteristic length of the potential
131 corresponds to the smallest distance at which the interaction changes sign, $V_{Li-Li}(\sigma_{Li-Li}) = 0$, and
132 is equal to $\sigma_{Li-Li} = 2.5668$ Å. The characteristic energy scale is defined by the depth of the first
133 minimum, equal to $\epsilon_{Li-Li} \equiv V_{Li-Li}(3.06) = -887.9$ K.

134 The helium-helium interaction is considered to be of the Lennard-Jones (LJ) type, and it is
135 parameterised to accurately describe the system at the temperatures and pressures of interest which
136 are well beyond ambient conditions. From preliminary simulations, we have found that the Aziz II
137 potential model[31], which is known to provide an excellent description of superfluid liquid helium
138 at temperatures close to absolute zero and moderate pressures around saturation density, does not
139 apply quite well at temperatures as high as 843 K and pressures in the GPa regime considered in the
140 present study when combined with the Li-Li model given above (Eq. 7). Instead, we retain the same
141 width $\sigma_{He-He} = 2.556$ Å but treat the potential depth ϵ_{He-He} as a free adjustable parameter. In this
142 work we have found that, in order to be able to reproduce the nucleation process, the depth must
143 be increased to the typical values of the Li-Li potential (Eq. 7). In order to test the influence of this
144 interaction parameter, we considered two different values of the potential depth, $\epsilon_{He-He} = -1200$ K
145 and $\epsilon_{He-He} = -800$ K, henceforth referred to as "model 1" and "model 2", respectively.

146 Finally, the helium-lithium interaction is modelled by a truncated Lennard-Jones potential at
147 short distances, namely a "hard" wall where we have basically eliminated the attractive part, with
148 characteristic parameters given by the Lorentz-Berthelot rules obtained from the corresponding
149 Li-Li and He-He values, and a cutoff beyond that point. This results in $\sigma_{Li-He} = 2.5615$ Å and
150 $\epsilon_{Li-He} = -1032.2$ K. The potential model is given by:

$$
\begin{aligned}
V_{Li-He}(r) &= 4\epsilon_{Li-He}\left[\left(\frac{\sigma}{r}\right)^{12} - \left(\frac{\sigma}{r}\right)^{6}\right], \quad r \le \sigma_{Li-He} \\
&= 0, \quad r > \sigma_{Li-He}
\end{aligned}
\tag{8}
$$

151 The four considered pairwise interactions are shown in Fig. 2. In a very recent work [32], it has been
152 reported that specific interatomic potentials based on Daw-Baskes and Finnis-Sinclair formalisms are
153 able to describe the formation of helium bubbles in a palladium tritide lattice at temperatures of the
154 order of 400 K and pressures in the range of 0.1 to 2.2 GPa. Furthermore, the formation of helium
155 bubbles in tungsten was also reproduced using purely repulsive He-W interaction potentials in cluster
156 simulations[33], models rather close to the ones presented in this work.

157 *Monte Carlo and molecular dynamics methods*

158 We rely on MC and MD methods to perform a series of computer simulations of the system. Both
159 methods use the microscopic model introduced in the previous section to describe the interactions
160 between the atoms as an input.

161 The Monte Carlo method has been used to obtain the equilibrium properties at fixed pressure
162 P, particle number N and temperature T. Calculations are performed starting from the microscopic
163 Hamiltonian of Eq. (6), using it to define the probability of a state with energy E according to the
164 Maxwell-Boltzmann distribution, $p = \exp(-E/k_B T)$, which is sampled using the standard Metropolis
165 algorithm. Once the system has been equilibrated, we perform simulations to estimate quantities of
166 interest such as the energy per particle and the volume, as well as correlation functions such as the pair
167 distribution function and the low-momentum static structure factor. An advantage of the MC method
168 is that it only uses the particle positions, in contrast to MD where their velocities have also to be
169 sampled. This halves the number of microscopic variables to estimate, thus reducing the phase space
170 and making the exploration more efficient. This, however, comes at a price: since Monte Carlo can
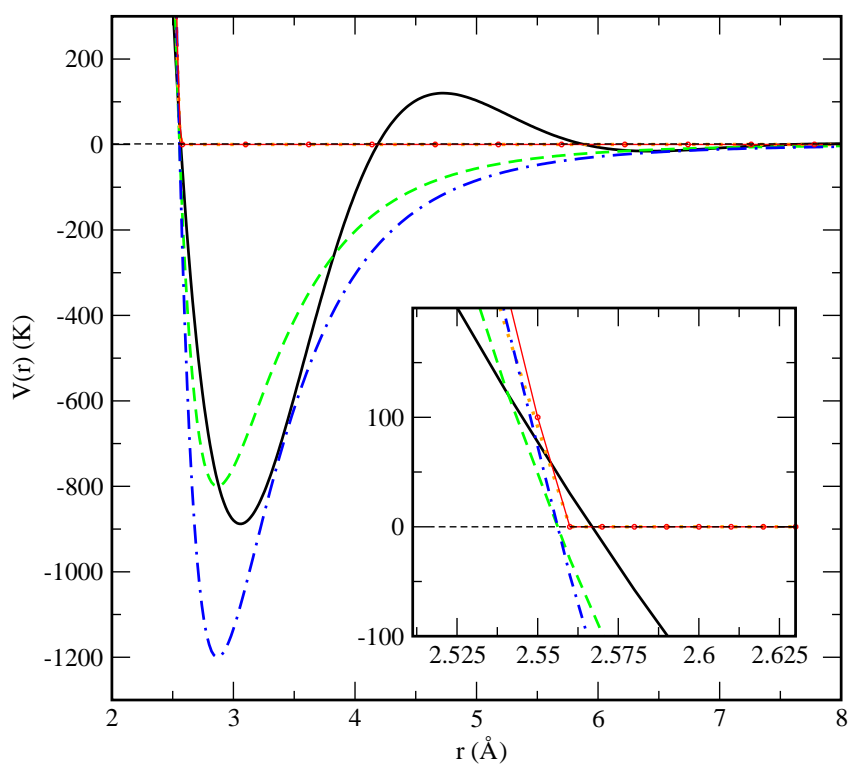
Figure 2. Microscopic two-body interaction potentials employed in this work. Main figure: overall view of the interaction potentials $V(r)$. Li-Li (black line); He-He model 1 (dot-dashed blue line); He-He model 2 (dashed green line); Li-He model 1 (red circles) and Li-He model 2 (dotted orange lines). The inset represents a zoom of the "hard-wall" area at short distances.

only sample equilibrium configurations it is not able to provide information about the time-dependent properties, in contrast to MD where the simulation propagates in real time.

In molecular dynamics, the force fields are also obtained from the model in Eq. (6) and the corresponding Newton's equations of motion, which are integrated numerically using a standard leap-frog Verlet procedure[34]. In each simulation, we fix the number of particles N and the pressure P, while the volume is adjusted accordingly. In addition to the energetic and structural properties obtained also in MC, MD provides access to time-dependent quantities such as the diffusion coefficient, velocity autocorrelation functions and spectral densities. As a stringent test of self-consistency, strict agreement between the common quantities sampled in MC and MD has to be obtained, which requires the proper thermalization and averaging in both methods.

3. Results and discussion

In all cases a homogeneous mixture of helium and lithium has been considered as the starting point of the simulations. The concentration of helium has been set to ~0.04 for a total of 40 helium atoms dissolved in a sea of 960 lithium atoms. The main results for the thermodynamic quantities of interest obtained in both MC and MD are summarised in Table 1. Additional simulations at intermediate pressures (0.3 and 0.4 GPa for instance) have also been considered in several other sections of the manuscript.

Table 1. Average internal energies (U), pressures (P) and temperatures (T) for the simulated setups. All MC simulations considered 10^8 sampling moves and all MD simulations were of total length 200 ps.

Method	U(K)	P (GPa)	T(K)
MC	71.1	0.104	843
	-187.0	0.122	843
	-430.3	0.146	843
	-553.3	0.178	843
	-700.0	0.208	843
	-1183.7	0.500	843
	-1398.6	1.005	843
	-1197.6	5.002	843
	-261.9	9.994	843
MD	150.8	0.105	842.3
	-214.2	0.128	842.1
	-380.4	0.152	842.1
	-507.6	0.177	842.1
	-720.8	0.202	841.9
	-1182.3	0.501	841.7
	-1405.2	0.999	841.6
	-1199.1	4.999	841.0
	-262.8	9.998	840.3

As a starting point of our analysis, we have obtained the average internal energies and pressures, as reported in Table 1. In the MC simulations, the system was initially allowed to equilibrate for a total of 10^7 MC random movements. The statistics was collected over the subsequent 10^8 random steps. In the case of MD, we employed a total time of about 50 ps for the equilibration of each system and later on we collected MD trajectories 200 ps long in all cases to compute meaningful physical properties. In both MC and MD the statistical errors were less than 1% in all reported quantities. The state of lowest internal energy is found at the pressure of 1 GPa. As an additional test, and in order to explore the influence of the helium concentration on the total energy of the system, we report energies as a function of the relative helium concentrations in Figure 3. We define the relative helium concentration p as

$$p = \frac{n_{\text{Li}} - n_{\text{He}}}{n_{\text{Li}} + n_{\text{He}}} \tag{9}$$

and observe a monotonic behaviour at the lowest pressure (0.1 GPa), while it becomes non-monotonic for the second pressure (0.3 GPa). This might be an indication of a different qualitative phase coexistence for the two selected pressures. We report further information about this aspect in the following sections.
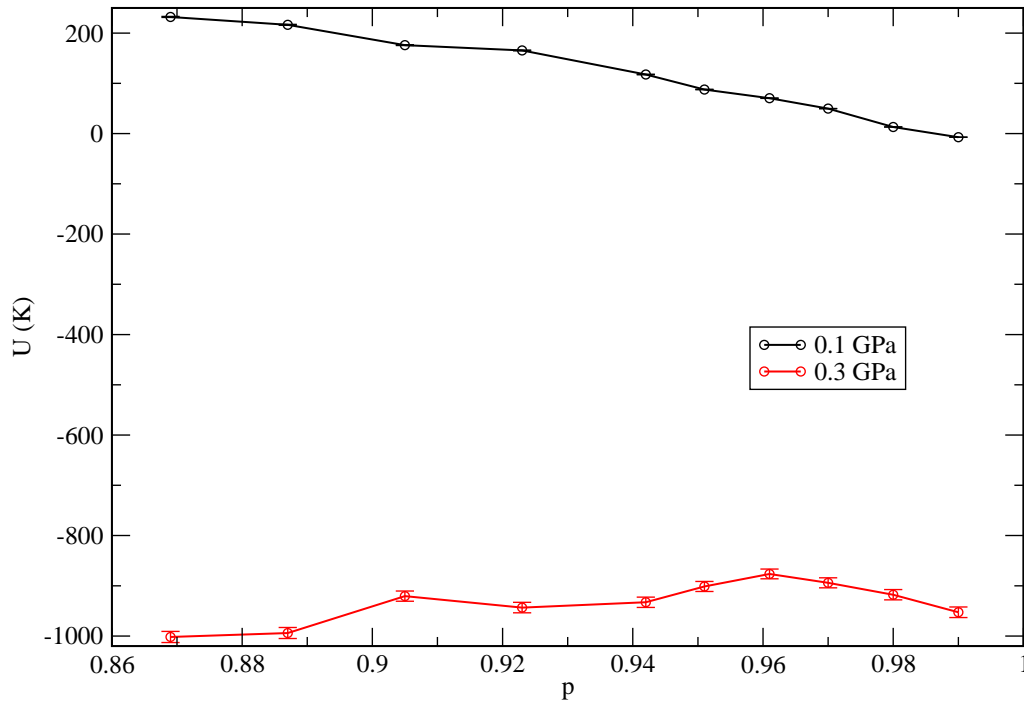

Figure 3. Total internal energies U as a function of concentration p for two characteristic pressures (0.1-0.3 GPa).

It has been reported in Ref.[35] that the solubility of helium in lithium is $\sim 5 \times 10^{-7}$ mol/$(1 \cdot \text{bar})$ at the pressure of 2.38 bar for temperatures in the range of 922 K — 1144 K, which is in agreement with Henry's law. At the same time, one should keep in mind that Henry's law is based on the assumption that the system behaves as an ideal gas and describes the overall incompressibility of liquid metals. Such a low solubility value means that, when applied to the typical conditions of our simulations (pressure of 1 GPa inside a volume of 24.26 nm^3, see Fig. 4), only around 0.06 helium atoms would be able to dissolve.

This explains why simulations performed at 843 K and high pressures (helium inverse densities are within the cubic nanometer range) are able to capture the phenomenon of helium nucleation, where helium cannot dissolve. Conversely, at lower pressures helium is able to dissolve in lithium. Furthermore, at the very high densities and pressures inside the projected nuclear fusion facilities Henry's law is rather unlikely to apply due to large deviations from the ideal gas behaviour. Figure 3 reports dependence of the specific volume (defined as the inverse of the density n^{-1}) on the pressure. One can see that the pressure rapidly increases as the specific volume is diminished, and that a plateau

216 is reached once the mean interparticle distance $n^{-1/3}$ becomes comparable to the hard-core size σ. At
217 that point the pressure can increase without a significant change in the density resulting in a vanishing
218 compressibility

$$\kappa = -\frac{1}{V}\frac{\partial V}{\partial P} = -\frac{1}{n^{-1}}\frac{\partial n^{-1}}{\partial P} \to 0, \quad P \to \infty . \tag{10}$$

219 On the other hand, the observed asymptotic incompressibility of lithium is in overall agreement with
220 Henry's law.
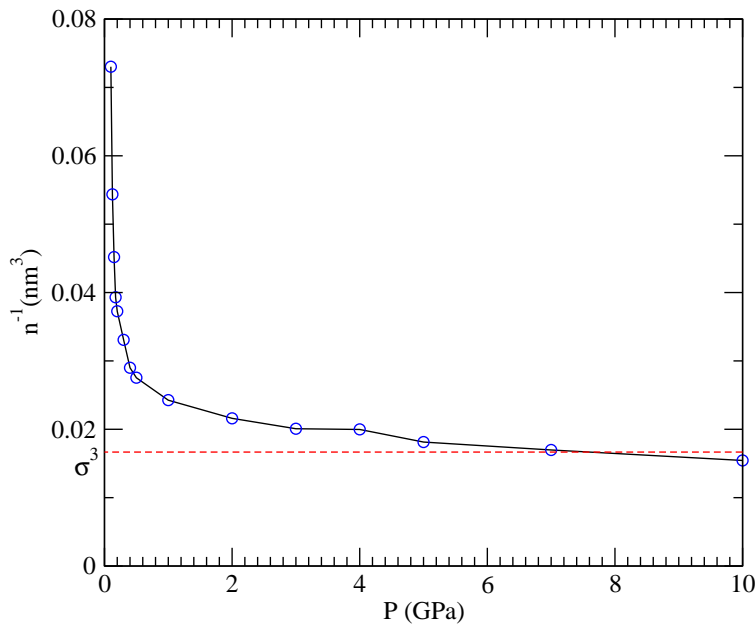
Figure 4. Specific volume n^{-1} as a function of the pressure in a wide range of pressures P (0.1—10 GPa).
Symbols: results of the simulation, with the error bars smaller than the symbol size. Dashed line:
hard-wall volume associated with the Van der Waals radius σ of lithium and helium (both are ~ 2.5 Å).

221 *3.1. Structure: Pair distribution function and structure factor*

222 In order to quantify the spatial correlations and visualise the structure of helium droplets, we
223 evaluate the pair distribution function $g(r)$ (RDF) in the simulated mixture of 960 Li and 40 He atoms
224 at 843 K. The RDF quantifies the probability of finding two atoms of species α and β at a distance r,

$$g_{\alpha,\beta}(r) = \frac{1}{N_\alpha N_\beta}\sum_{i=1}^{N_\alpha}\sum_{j=1}^{N_\beta}\langle\delta(|\mathbf{r}|_{ij} - r)\rangle , \tag{11}$$

225 where $\langle\cdots\rangle$ denotes a thermal average. Being a two-particle correlator, the RDF is capable of
226 capturing a translationally invariant ordering and is therefore suitable to identify droplet formation
227 independently of its center of mass position. Typical RDF functions for Li-Li, Li-He and He-He
228 pairs are shown in Fig. 5 for different pressures. The shape of the Li-Li pair distribution functions is

229 characteristic of a liquid at equilibrium. The Li-Li RDFs are hardly affected by the presence of a small
230 concentration of helium atoms, as it can be seen in comparison with the behaviour of pure lithium
231 at 1 GPa and the same temperature, taken from Ref. [30]. One might also note that a change of two
232 orders of magnitude in the pressure does not significantly affect the overall shape of $g_{Li-Li}(r)$. The
233 short-range region is voided due to the steep hard-core potential. High-amplitude oscillations appear
234 at separations comparable to the mean interparticle distance and witness strong correlations in the
235 liquid that can be interpreted as shell effects.
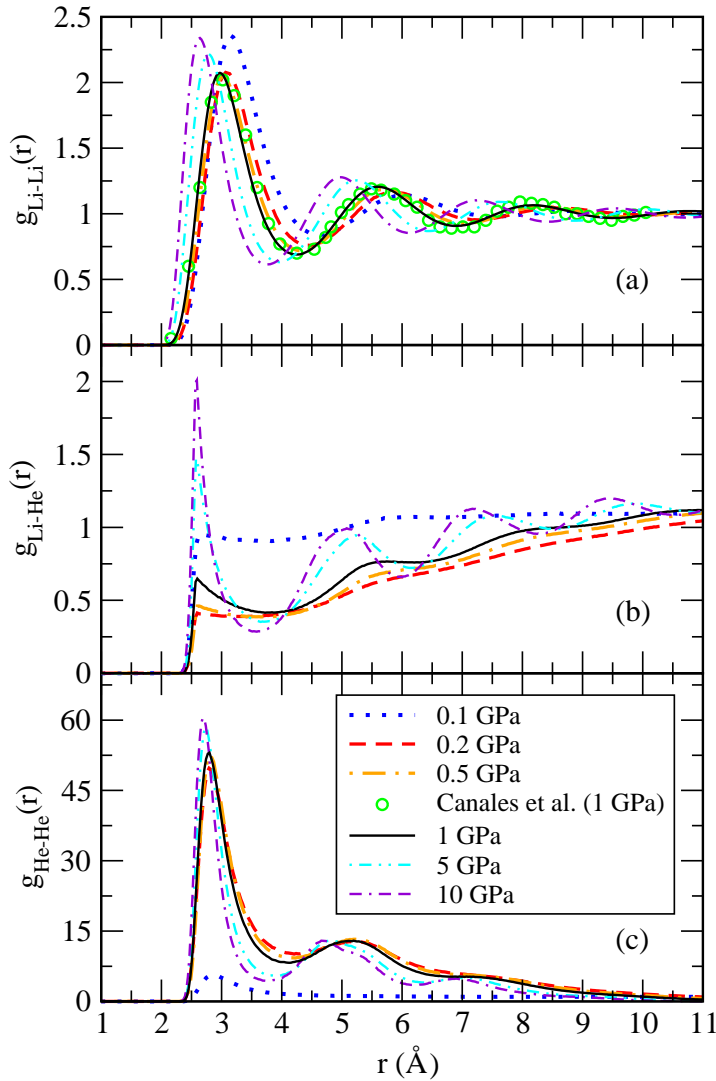
Figure 5. Pair distribution functions in a wide range of pressures (0.1-10 GPa) quantifying (a) He-He
(b) He-Li (c) Li-Li correlations. Green circles, single-species Li-Li data from Ref. [30]. Lines: 0.1 GPa
(dotted blue); 0.2 GPa (dashed red); 0.5 GPa (dot-dashed orange); 5 GPa (dot-dot-dashed cyan); 10 GPa
(dash-dash-dotted violet).

236   At large distances, the pair distribution function approaches a constant value, thus confirming
237 that lithium atoms are homogeneously filling the whole space. The situation is drastically different
238 in the He-He RDFs, as they vanish at large distances as seen in Fig. 5(c). While at low pressure,
239 g_{He-He} still shows a long-range plateau, this is not the case for large pressure where the RDF strongly
240 decreases. This implies that helium atoms bunch up close to each other, thus forming droplets. In
241 this way, helium atoms form a miscible mixture on a lithium background at low pressure, but have a

tendency to phase separate at large pressures, splitting the system into pure lithium and helium phases. This scenario is further supported by the massive increase in the height of the first and subsequent shells in a He droplet. The droplet size can be roughly estimated as the difference between the distance at which $g_{\text{He}-\text{He}}(r)$ significantly decays (taken from the first minimum) and the position of the starting non-zero value of the RDF.

In order to verify the robustness of our analysis, we have compared the results obtained with the two different He-He potential models proposed (see Section 2) corresponding to a depth well of 800 K and 1200 K, to find only minor changes. We have observed that when this depth is below 650 K, long-lived helium droplets are not formed and become significantly unstable in short time intervals of the order of 1 ps. From here on, the reported results correspond to model 1, as it predicts more stable helium droplets.
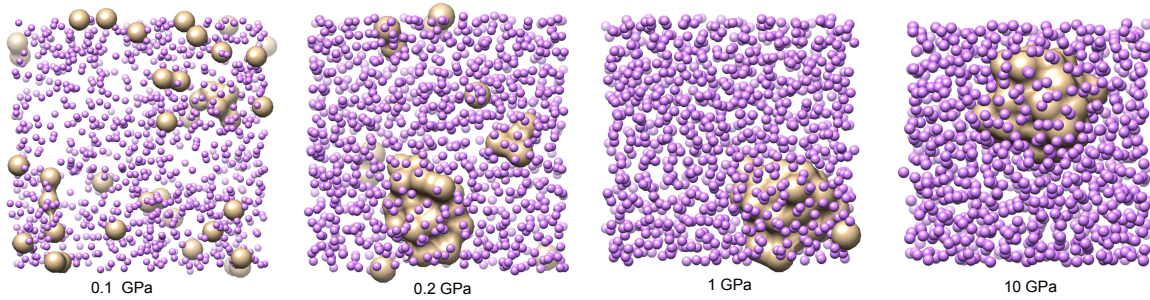
Figure 6. Snapshots of the He-Li mixtures at characteristic pressures: 0.1 GPa, 0.2 GPa, 1 GPa, 10 GPa.

A set of four characteristic snapshots of the system at pressures $P = 0.1, 0.2, 1$ and 10 GPa is shown in Fig. 6 to illustrate the tendency of the system to form helium droplets when the pressure is increased above approximately 0.2 GPa. At the lowest pressures considered helium is uniformly diluted in the lithium bath, showing that only small clusters of the size of a few helium units appear. This is also seen in the He-He pair distribution function, which is shown in Fig. 7 for several values of P close to the critical transition pressure. We observe that larger helium droplets start to form at a crossover pressure around 0.175 GPa, which corresponds to phase separation (helium droplets in liquid lithium), and fully stable ones appear at 0.2 GPa. A possible explanation of this effect can be based on the behaviour of the binding (cohesive) potential energy of helium

$$U_{binding} \equiv \frac{U_{He-Li} - U_{Li}}{N_{He}} \tag{12}$$

where U_{He-Li} and U_{Li} stand for the internal energies of the mixture and pure lithium, respectively and N_{He} is the total number of helium atoms, fixed to 40 in this work. The obtained results are reported in Table 2. Here, the values of U_{Li} have been extracted from additional simulations of pure lithium at 0.1, 1 and 10 GPa. We find that the cohesive potential energy is positive at low pressures where the lithium atoms prefer not to bind, while it becomes negative at large pressures, where formation of large lithium droplets is observed. Thus, the stability of the helium droplets is significantly enhanced at high pressures.

Table 2. Binding energies of helium at 800 K as a function of the pressure.

Pressure (GPa)	U_{He-Li} (K)	U_{Li} (K)	$U_{binding}$ (K)
0.1	110	-58	4.2
1	-1402	-1413	0.275
10	-262	-188	-1.85

A possible effect that could be expected is the formation of aggregates of lithium and helium due to van der Waals forces[36]. However, we have not observed that pairing in our simulations, as it can be seen from the Li-He RDF of Fig.5. This is probably due to the short-range repulsive He-Li interactions considered, as shown in Eq. 8.
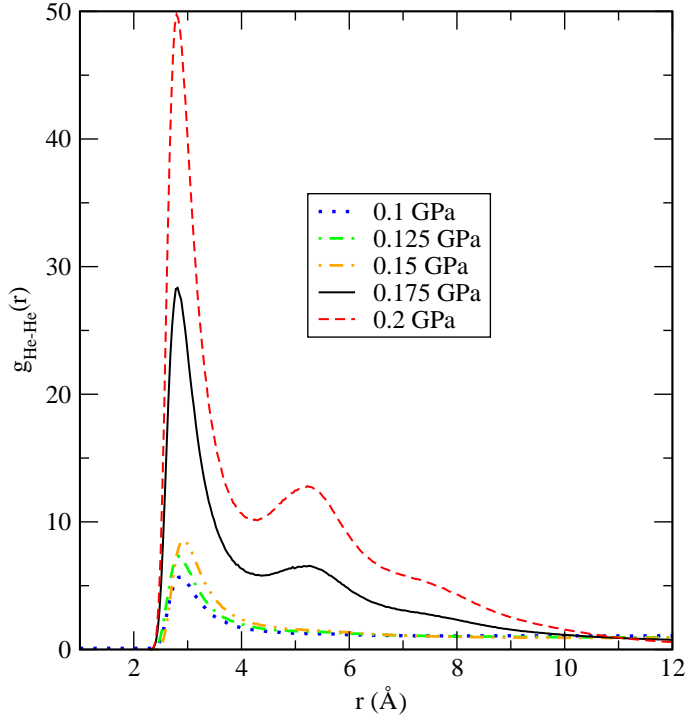

Figure 7. He-He pair distribution functions in the vicinity of the phase-separation transition (0.1—0.2 GPa). Lines: 0.1 GPa (dotted blue); 0.125 GPa (dot-dashed green); 0.15 GPa (dot-dot-dashed orange); 0.175 GPa (black); 0.2 GPa (dashed red).

In order to further characterise the phase separation, we also report static structure factors $S(k)$ computed from the RDF (Eq. 11) at low momenta ($k = 0.216$ $^{-1}$) as a function of the pressure (see for instance[37]):

$$S(k) = 1 + \frac{4\pi\rho_0}{k} \int_0^\infty \mathrm{d}r \, r \, [g(r) - 1] \sin kr, \tag{13}$$

where ρ_0 is the density of a pure species or the average ($\sqrt{\rho_{Li}\rho_{He}}$) for the Li-He pair correlation. The results are shown in Fig. 8. The change in the slope of $S(k)$ is particularly sharp in the He-He case, around the crossover pressure of 0.175 GPa, as opposed to what happens in the Li-Li and Li-He cases. It has recently been reported [38] that the sensibility of changes in the slope of the static structure factors may be a clear indication of a possible phase transition between a helium drop and a mixture of helium dissolved in lithium. The precise quantification of such a phase transition is currently evaluated in our lab, although it is out of the scope of the present work.

The radii of the helium droplets formed in our simulations are reported in Table 3 and represented in Fig. 9 while the specific size depends on the number of particles in the simulation. We considered only the reference case of 40 Helium and 960 lithium atoms. One observes that the radius is largest
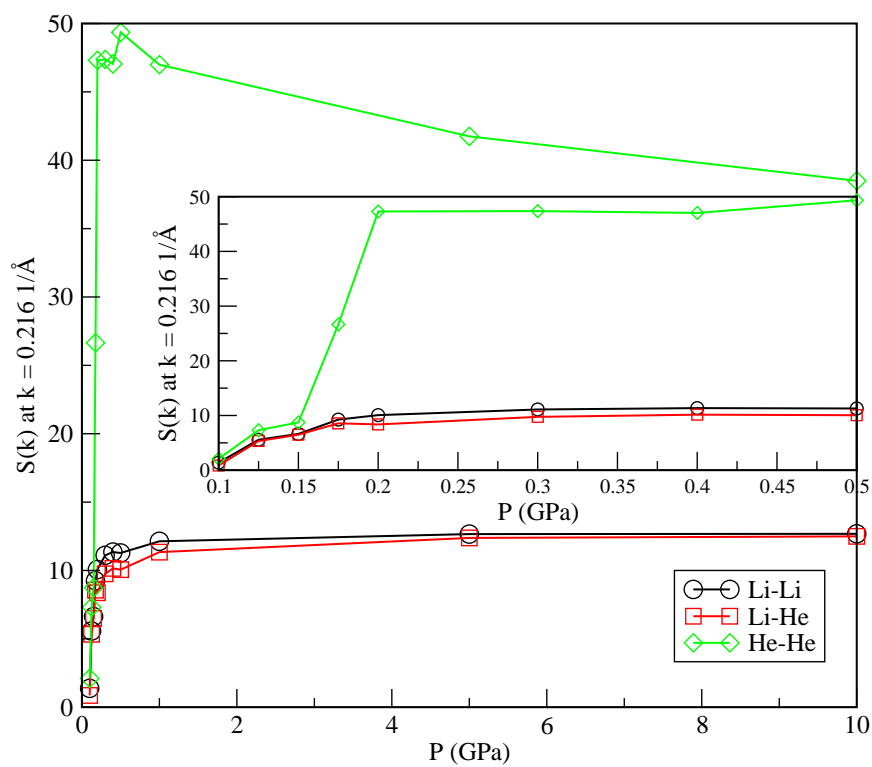
Figure 8. Static structure factors computed at very low momentum ($k = 0.2161/$) a function of the pressure. Li-Li (black circles); Li-He (red squares); He-He (green diamonds).

286 at low pressures thus decreasing as the pressure increases. At pressures below 1 GPa, we can fit an
287 exponential law: $R/\text{Å} = 1.965e^{-0.12P/\text{GPa}}$ whereas in the range above 1 GPa, the best fit is linear:
288 $R/\text{Å} = (1.84—0.05) P/\text{GPa}$. This indicates a qualitatively different behaviour for R that is strongly
289 dependent on the pressure.

Table 3. Radii of helium droplets at 843 K as a function of the pressure.

Pressure (GPa)	R_{He} (Å)
0.175	1.98
0.2	1.93
0.3	1.85
0.5	1.81
1	1.85
5	1.63
7	1.51
10	1.32
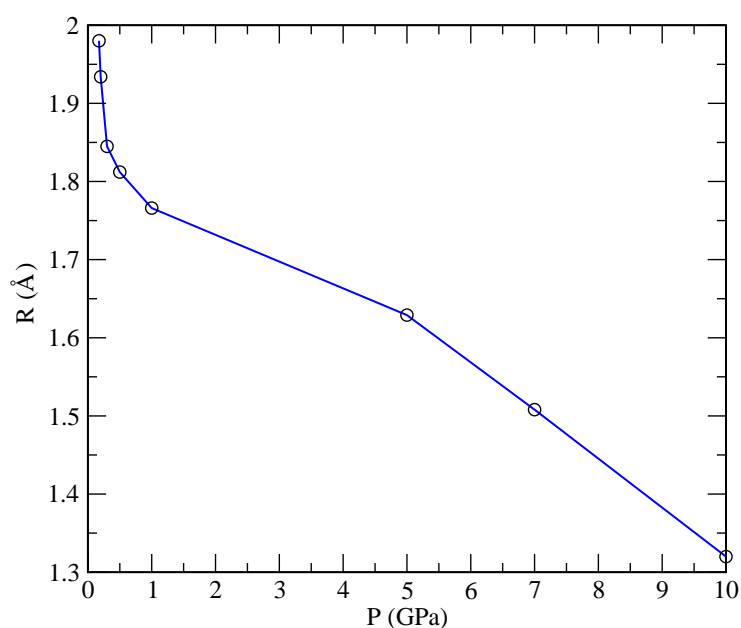
Figure 9. Radii of helium droplets for the pressure range 0.175-10 GPa.

290 *3.2. Dynamics: Atomic self-diffusion coefficients*

291   Another experimentally relevant quantity is the diffusion coefficient. We obtain the mean square
292 displacement (MSD) for both helium and lithium from the MD simulations. The value of the diffusion
293 coefficient D is then computed from the slope of the steady-state MSD curve, using Einstein's formula

$$D = \frac{1}{6} \lim_{t \to \infty} \frac{\mathrm{d}}{\mathrm{d}t} \langle |\mathbf{r}(t) - \mathbf{r}(0)|^2 \rangle, \tag{14}$$

where $\mathbf{r}$ stands for the coordinate of each species. The coefficients for all simulated states are reported in Table 4. Canales et al. [30] obtained a value for the diffusion coefficient of pure lithium at 843 K (around 1 GPa) of 2.47 Å^2/ps, whereas Jayaram et al. [39] reported 0.8 Å^2/ps at 500 K. We get a similar value, $D = 2.0$ Å^2/ps at 843 K, indicating that the lithium diffusion coefficient does not change significantly from its value in the absence of helium. This is not surprising considering the low concentration of helium atoms in the regimes analysed. It is also worth noticing that a significantly higher experimental value of 45 Å^2/ps at 523 K, reported by Nieto et al. [40] for helium injected onto the surface of a stream of flowing lithium, was obtained in a system out of equilibrium, which is a different situation from the one analysed here. This can explain the large difference of about two orders of magnitude when compared to our result, 0.833 Å^2/ps at 843 K and 1 GPa (see Table 4). Experiments in similar systems might provide a more suitable reference to compare our results to. Figure 10 shows the dependence of D obtained in our simulations as a function of the pressure. As it can be seen, the dependence of D on P is approximately linear, with a slower diffusion at pressures above 1 GPa.

Table 4. Diffusion coefficients of lithium and helium at 843 K as a function of the pressure.

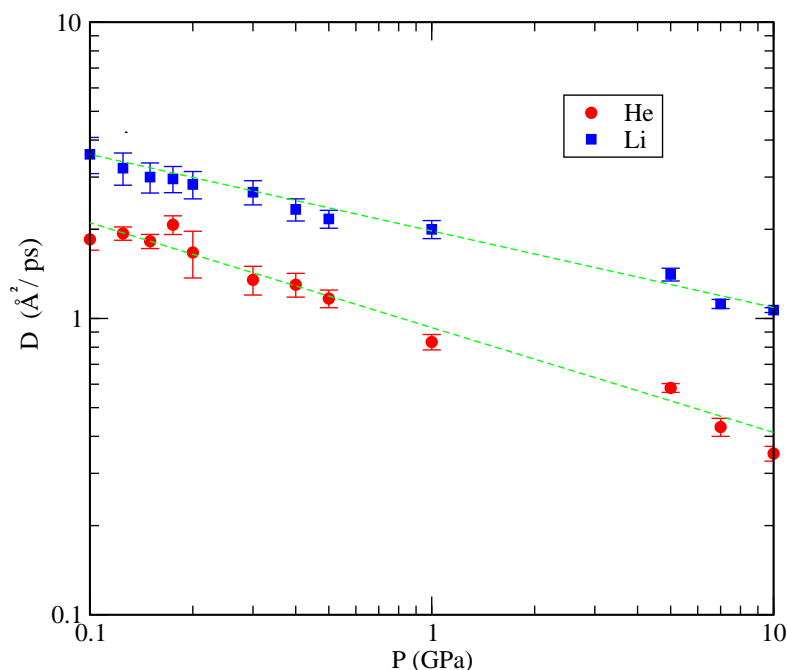| Pressure (GPa)	D_{He} (Å^2/ps)	D_{Li} (Å^2/ps)
0.1	1.850	3.583
0.125	1.936	3.217
0.15	1.822	3.010
0.175	2.071	2.958
0.2	1.670	2.833
0.3	1.350	2.667
0.4	1.300	2.333
0.5	1.167	2.167
1	0.833	2.006
5	0.583	1.408
7	0.430	1.120
10	0.350	1.067

Figure 10. Diffusion coefficients of lithium (blue squares) and helium (red circles) at 800 K as a function of the of the pressure on a logarithmic scale. Green straight lines are a guide to the eye.

307 Experimental infrared spectra are usually obtained from the absorption coefficient $\alpha(\omega)$ or the
308 imaginary part of the frequency-dependent dielectric constant[41]. These properties are directly related
309 to the absorption lineshape $I(\omega)$, which can also be obtained in molecular dynamics simulations[42,43].
310 In most cases the physically relevant property to be computed is the so-called atomic spectral density
311 $S_i(\omega)$:

$$S_i(\omega) = \int_0^\infty dt\ \langle \vec{v}_i(t)\vec{v}_i(0) \rangle\ \cos(\omega t), \tag{15}$$

312 where $\vec{v}_i(t)$ is the velocity of the $i-th$ atom at time t, while the brackets $\langle \cdots \rangle$ denote an equilibrium
313 ensemble average. In our case we have obtained the spectral density of each atomic species
314 separately. Generally speaking, classical molecular dynamics simulations are not able to fully
315 reproduce experimental absorption coefficients, these being quantum properties. However they
316 can be used to locate the position of the spectral bands since in the harmonic (oscillator) approximation,
317 the classical and quantum ground state frequencies are equal.
318 The power spectrum describes the main vibrational modes of a molecular system, including low
319 frequencies below 100 ps^{-1},associated with translational and rotational modes, and high frequencies
320 of stretching and bending vibrations around and above 500 ps^{-1}. The power spectra were obtained for
321 the velocity autocorrelation functions of lithium and helium atoms and are reported in Fig. 11. We
322 find that lithium atoms have a tendency to oscillate at frequencies between 30 and 85 ps^{-1}, whereas
323 the vibrational frequency for helium atoms is between 2 and 100 ps^{-1}, approximately. The fact that
324 these peaks are found at low frequencies is consistent with a picture where the atoms can only present
325 translational vibration modes, mainly associated with the restricted translations often referenced

326 to as the *cage effect*. These are typical of most condensed liquids and in the present case due to
327 short-range interactions of a given lithium or helium atom with its closest neighbours[44]. As a general
328 trend, we observe that translational modes decrease their values as pressure rises, as expected due to
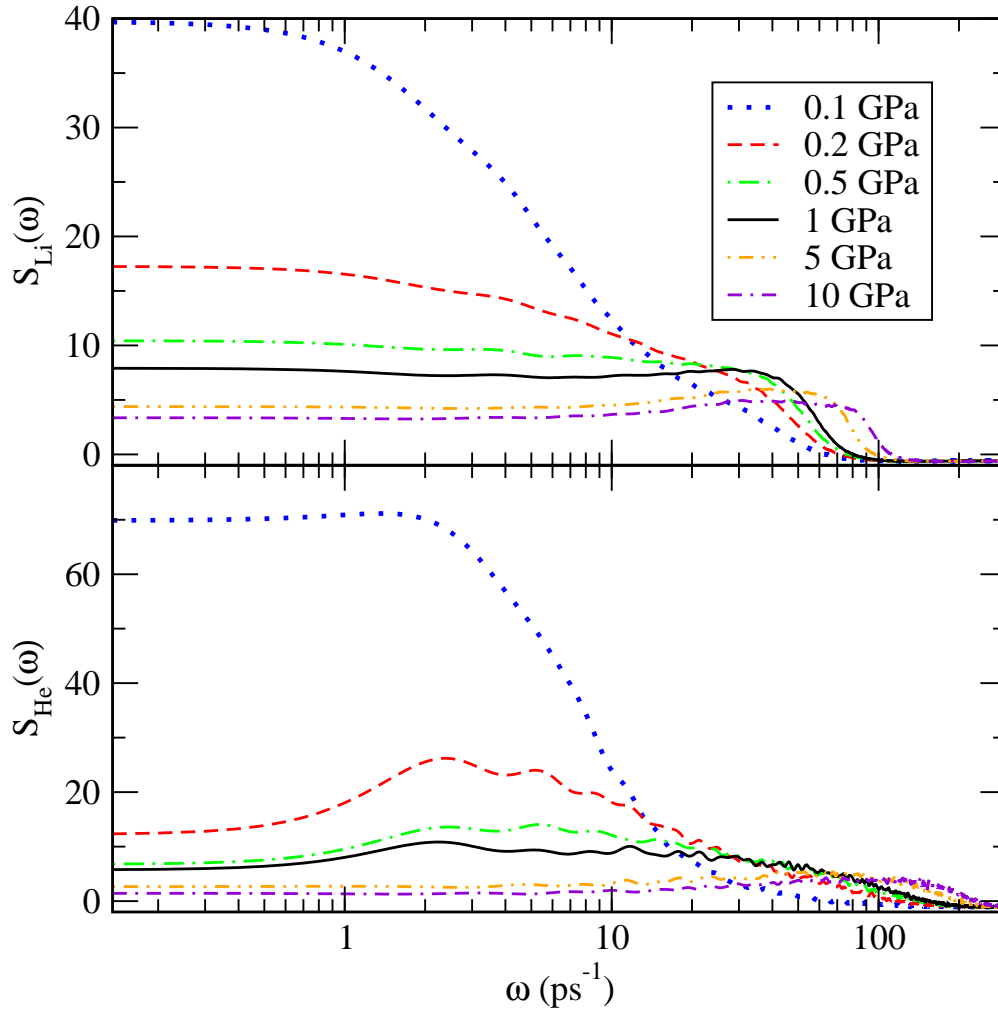329 condensation effects.

Figure 11. Spectral densities of lithium (top) and helium (bottom) at 843 K as a function of pressure. Lines: 0.1 GPa (dotted blue); 0.2 GPa (dashed red); 0.5 GPa (dot-dashed green); 1 GPa (black); 5 GPa (dot-dot-dashed orange); 10 GPa (dash-dash-dotted violet).

4. Conclusions

331 In this work we have analysed the structure and dynamics of lithium-helium mixtures with a very
332 low He concentration as a first step towards the simulation of the typical environmental conditions in
333 the BB of a fusion power plant. We perform classical simulations of the lithium-helium mixture using
334 Monte Carlo and molecular dynamics methods, both yielding the same predictions at equilibrium.

Monte Carlo approach is more efficient for the calculation of thermodynamic quantities and we employ it for the estimation of the total energy and pressure, along with some of its structural properties as the pair distribution functions. In addition, molecular dynamics is used to obtain time-dependent quantities such as the diffusion coefficients, velocity autocorrelation functions and power spectra of the atoms in the mixture.

In our simulations we have observed that lithium becomes incompressible at pressures above 2 GPa, in overall agreement with Henry's law. At the same time, the helium solubility is too low in the range of high pressures considered so we observe the formation of helium droplets within our microscopic model. Furthermore, we also find that helium atoms are miscible in the lithium bath at low pressures.

The simulations reported in this work provide a first step towards the understanding of the phenomenon of helium nucleation in liquid lithium directly from a microscopic model. We have shown that at high temperatures and high pressures this can be captured by classical computer simulations at its inception if appropriate potential models are used. Independently of the initial homogeneous disposition of atoms in the system, our simulations show the formation of helium droplets systematically if the same environmental conditions are met. Dynamical properties of the mixture, such as diffusion coefficients of lithium and helium, are very well reproduced, in overall good agreement with the experimental and computational data available. Future studies would likely involve the calculation of surface tensions of the droplets and the analysis of the nucleation phenomenon on lithium-lead-helium mixtures in the range of high temperatures and pressures.

Author Contributions: Data curation, J.Martí, F.Mazzanti, G.E.Astrakharchik, L.Batet, B.Pedreño; formal analysis, J.Martí, F.Mazzanti, G.E.Astrakharchik, L.Batet, L.Portos-Amill, B.Pedreño; funding acquisition, J.Martí, F.Mazzanti, G.E.Astrakharchik, L.Batet; investigation, J.Martí, F.Mazzanti, G.E.Astrakharchik, L.Batet, L.Portos-Amill, B.Pedreño; project administration, J.Martí, F.Mazzanti, G.E.Astrakharchik, L.Batet; software, , J.Martí, L.Portos-Amill, B.Pedreño; supervision, J.Martí, F.Mazzanti, G.E.Astrakharchik, L.Batet,; writing–original draft preparation, J.Martí, F.Mazzanti, G.E.Astrakharchik, L.Batet; writing–review and editing, J.Martí, F.Mazzanti, G.E.Astrakharchik, L.Batet.

Conflicts of Interest: The authors declare no conflict of interest.

Abbreviations

The following abbreviations are used in this manuscript:

BB	breeding blanket
CNT	classical nucleation theory
LM	liquid metal
LLE	lithium-lead eutectic
MC	Monte Carlo simulations
MD	molecular dynamics simulations
RDF	radial distribution function
MSD	mean square displacement

References

1. Kordač, M.; Košek, L. Helium bubble formation in Pb-16Li within the breeding blanket. *Fusion Engineering and Design* **2017**, *124*, 700–704.

2.   Federici, G.; Boccaccini, L.; Cismondi, F.; Gasparotto, M.; Poitevin, Y.; Ricapito, I. An overview of the EU breeding blanket design strategy as an integral part of the DEMO design effort. *Fusion Engineering and Design* **2019**, *141*, 30–42.

3.   Rubel, M. Fusion neutrons: tritium breeding and impact on wall materials and components of diagnostic systems. *Journal of Fusion Energy* **2019**, *38*, 315–329.

4.   Coen, V. Lithium-lead eutectic as breeding material in fusion reactors. *Journal of nuclear materials* **1985**, *133*, 46–51.

5.   De Les Valls, E.M.; Sedano, L.; Batet, L.; Ricapito, I.; Aiello, A.; Gastaldi, O.; Gabriel, F. Lead–lithium eutectic material database for nuclear fusion technology. *Journal of nuclear materials* **2008**, *376*, 353–357.

6.   Sedano, L. Helium Bubbles Cavitation Phenomena in Pb-15.7 Li and Potential Impact on Tritium Transport Behaviour in HCLL Breeding Channels. Technical Report, Centro de Investigaciones Energeticas Medioambientales y Tecnologicas (CIEMAT), 2007.

7.   Ruzic, D.; Szott, M.; Sandoval, C.; Christenson, M.; Fiflis, P.; Hammouti, S.; Kalathiparambil, K.; Shchelkanov, I.; Andruczyk, D.; Stubbers, R.; others. Flowing liquid lithium plasma-facing components–Physics, technology and system analysis of the LiMIT system. *Nuclear Materials and Energy* **2017**, *12*, 1324–1329.

8.   Smolentsev, S.; Rognlien, T.; Tillack, M.; Waganer, L.; Kessel, C. Integrated Liquid Metal Flowing First Wall and Open-Surface Divertor for Fusion Nuclear Science Facility: Concept, Design, and Analysis. *Fusion Science and Technology* **2019**, *75*, 939–958.

9.   Nakamura, H.; Agostini, P.; Ara, K.; Cevolani, S.; Chida, T.; Ciotti, M.; Fukada, S.; Furuya, K.; Garin, P.; Gessii, A.; others. Latest design of liquid lithium target in IFMIF. *Fusion Engineering and Design* **2008**, *83*, 1007–1014.

10. Gibbs, J.W. On the equilibrium of heterogeneous substances. *American Journal of Science* **1878**, *3*, 441–458.

11. Gibbs, J.W. *Scientific Papers of J. Willard Gibbs, in Two Volumes*; Vol. 1, Longmans, Green, 1906.

12. Batet, L.; Fradera, J.; de les Valls, E.M.; Sedano, L. Numeric implementation of a nucleation, growth and transport model for helium bubbles in lead–lithium HCLL breeding blanket channels: Theory and code development. *Fusion engineering and design* **2011**, *86*, 421–428.

13. Frenkel, J. *Kinetic Theory of Liquids*; Oxford Univ. Press, New York, 1946.

14. Gunton, J. Homogeneous nucleation. *Journal of statistical physics* **1999**, *95*, 903–923.

15. Yakimovich, K.A.; Mozgovoi, A.G. Experimental investigation of the density and surface tension of molten lithium at temperatures up to 1300 K. *High Temperature* **2000**, *38*, 657–659.

16. Mazzanti, F.; Polls, A.; Boronat, J.; Casulleras, J. High-Momentum Response of Liquid He3. *Physical review letters* **2004**, *92*, 085301.

17. Pierleoni, C.; Morales, M.A.; Rillo, G.; Holzmann, M.; Ceperley, D.M. Liquid–liquid phase transition in hydrogen by coupled electron–ion Monte Carlo simulations. *Proceedings of the National Academy of Sciences* **2016**, *113*, 4953–4957.

18. Bombin, R.; Boronat, J.; Mazzanti, F. Dipolar Bose supersolid stripes. *Physical review letters* **2017**, *119*, 250402.

19. Sánchez-Baena, J.; Boronat, J.; Mazzanti, F. Supersolid stripes enhanced by correlations in a Raman spin-orbit-coupled system. *Physical Review A* **2020**, *101*, 043602.

20. Padro, J.; Martí, J.; Guàrdia, E. Molecular dynamics simulation of liquid water at 523 K. *Journal of Physics: Condensed Matter* **1994**, *6*, 2283.

21. Nagy, G.; Gordillo, M.; Guàrdia, E.; Martí, J. Liquid water confined in carbon nanochannels at high temperatures. *The Journal of Physical Chemistry B* **2007**, *111*, 12524–12530.

22. Calero, C.; Martí, J.; Guàrdia, E. 1H nuclear spin relaxation of liquid water from molecular dynamics simulations. *The Journal of Physical Chemistry B* **2015**, *119*, 1966–1973.

23. Zambrano, H.A.; Walther, J.H.; Koumoutsakos, P.; Sbalzarini, I.F. Thermophoretic motion of water nanodroplets confined inside carbon nanotubes. *Nano letters* **2009**, *9*, 66–71.

24. Videla, P.; Sala, J.; Martí, J.; Guàrdia, E.; Laria, D. Aqueous electrolytes confined within functionalized silica nanopores. *The Journal of chemical physics* **2011**, *135*, 104503.

25. Karplus, M.; McCammon, J. Molecular dynamics simulations of biomolecules. *Nature structural biology* **2002**, *9*, 646–652.

26. Yang, J.; Calero, C.; Martí, J. Diffusion and spectroscopy of water and lipids in fully hydrated dimyristoylphosphatidylcholine bilayer membranes. *The Journal of chemical physics* **2014**, *140*, 03B606_1.

27. Martí, J.; Csajka, F. The aqueous solvation of sodium chloride: A Monte Carlo transition path sampling study. *The Journal of Chemical Physics* **2000**, *113*, 1154–1161.

28. Bolhuis, P.G.; Chandler, D.; Dellago, C.; Geissler, P.L. Transition path sampling: Throwing ropes over rough mountain passes, in the dark. *Annual review of physical chemistry* **2002**, *53*, 291–318.

29. Canales, M.; Padró, J.; González, L.; Giró, A. Molecular dynamics simulation of liquid lithium. *Journal of Physics: Condensed Matter* **1993**, *5*, 3095.

30. Canales, M.; González, L.; Padró, J. Computer simulation study of liquid lithium at 470 and 843 K. *Physical Review E* **1994**, *50*, 3656.

31. Aziz, R.A.; McCourt, F.R.; Wong, C.C. A new determination of the ground state interatomic potential for He2. *Molecular Physics* **1987**, *61*, 1487–1511.

32. Zhou, X.; Bartelt, N.; Sills, R. Enabling simulations of helium bubble nucleation and growth: A strategy for interatomic potentials. *Physical Review B* **2021**, *103*, 014108.

33. Juslin, N.; Wirth, B. Interatomic potentials for simulation of He bubble formation in W. *Journal of Nuclear Materials* **2013**, *432*, 61–66.

34. Frenkel, D.; Smit, B. *Understanding molecular simulation: from algorithms to applications*; Vol. 1, Elsevier, 2001.

35. Slotnick, H. *The solubility of helium in lithium and potassium*; Vol. 380, Pratt & Whitney Aircraft Division, United Aircraft Corporation, CANEL Operations, 1965.

36. Al Taisan, N.A. *Spectroscopic detection of the lithium helium (LiHe) van der waals molecule*; University of Nevada, Reno, 2013.

37. Chandler, D. Introduction to modern statistical. *Mechanics. Oxford University Press, Oxford, UK* **1987**, *5*.

38. Wang, L. Discovering phase transitions with unsupervised learning. *Physical Review B* **2016**, *94*, 195105.

39. Jayaram, C.; Ravi, R.; Chhabra, R. Calculation of self-diffusion coefficients in liquid metals based on hard sphere diameters estimated from viscosity data. *Chemical physics letters* **2001**, *341*, 179–184.

40. Nieto, M.; Ruzic, D.; Allain, J.P.; Coventry, M.; Vargas-Lopez, E. Helium retention and diffusivity in flowing liquid lithium. *Journal of nuclear materials* **2003**, *313*, 646–650.

41. McQuarrie, D.A. *Statistical Mechanics*; University Science Books, 2000.

42. Martí, J.; Padró, J.; Guàrdia, E. Computer simulation of molecular motions in liquids: Infrared spectra of water and heavy water. *Molecular Simulation* **1993**, *11*, 321–336.

43. Praprotnik, M.; Janežič, D. Molecular dynamics integration and molecular vibrational theory. III. The infrared spectrum of water. *J. Chem. Phys.* **2005**, *122*, 174103.

44. Padró, J.; Martí, J. Response to "Comment on 'An interpretation of the low-frequency spectrum of liquid water'"[J. Chem. Phys. 118, 452 (2003)]. *The Journal of Chemical Physics* **2004**, *120*, 1659–1660.